# ARTICLE

## Resonant Amplification of Intrinsic Magnon Modes and Generation of New Extrinsic Modes in a Two-Dimensional Array of Interacting Multiferroic Nanomagnets by Surface Acoustic Waves

Anulekha De,[a] Justine Lynn Drobitch,[b] Saswati Barman,[c] Supriyo Bandyopadhyay, *[c] and Anjan Barman*[a]

We demonstrate surface-acoustic-wave (SAW) induced resonant amplification of intrinsic spin-wave (SW) modes, as well as generation of new extrinsic modes at the SAW frequency, in a densely packed two-dimensional array of elliptical Co nanomagnets fabricated on a piezoelectric LiNbO3 substrate. These modes are observed in the absence of any bias magnetic field. Micromagnetic simulation results are in good agreement with the experimental observations and elucidate the underlying dynamics. Our findings lay the groundwork for bias-field-free magnonics, where the SW behavior is efficiently tuned by SAWs. It has important applications in the design of energy efficient on-chip microwave devices, spin-wave logic, and extreme sub-wavelength ultra-miniaturized microwave antennas for embedded applications.

[a.] Department of Condensed Matter Physics and Material Sciences, S. N. Bose National Centre for Basic Sciences, Block JD, Sector-III, Salt Lake, Kolkata 700 106, India. Email: abarman@bose.res.in

[b.] Department of Electrical and Computer Engineering, Virginia Commonwealth University, Richmond, VA 23284, USA. Email: sbandy@vcu.edu

[c.] Institute of Engineering and Management, Sector V, Salt Lake, Kolkata, 700 091, India.

## Introduction

Magnetoelasticity (ME) or inverse magnetostriction has emerged as a powerful tool to couple magnons and phonons since the magnetization precession in ferromagnetic magnetostrictive materials is affected by elastic stress[1-5] and hence by surface acoustic waves (SAW)[6,7] which are propagating strain (elastic) waves consisting of acoustic phonons. SAW-induced precession of magnetization in magnetostrictive nanomagnets has been studied extensively[8, 9] and SAW-induced magnetization rotation and domain-wall motion in magnetostrictive nanomagnets have been harnessed for energy-efficient hybrid writing schemes for non-volatile memory. [10, 11] Over the last decade, SAW in the GHz frequency regime has been used to excite or manipulate spin waves (SWs) in magnetic thin films [2, 12] and nanostructures[13, 14] through ME interactions.

In this work, we demonstrate, using time-resolved magneto-optical Kerr effect (TR-MOKE) microscopy, that SAW can strongly influence the magnetization dynamics (and hence magnon modes) in a two-dimensional (2D) densely packed array of interacting elliptical magnetostrictive Co nanomagnets, fabricated on a piezoelectric 128° Y-cut $LiNbO_3$ substrate. This is a system of 2-phase (magnetostrictive + piezoelectric) multiferroic nanomagnets. The interplay between the demagnetizing field arising from the shape anisotropy of the nanomagnets and the dipolar coupling field generated by the strong magnetostatic inter-element interaction trigger incoherent magnetization precession within the array at zero bias magnetic field (remanent state) causing the emergence of intrinsic SW (magnonic) modes. We call them 'intrinsic modes' since they are intrinsic to the array and do not depend on any external bias magnetic field or other types of excitation like a SAW. When a SAW is launched into the 2D array, we observe two effects: (i) amplification of an existing (intrinsic) SW mode's power when the SAW frequency is resonant with that mode's frequency, and (ii) generation of a new extrinsic ME mode at the SAW frequency when the latter is not resonant with the frequency of any intrinsic mode. We call the new modes "extrinsic" since they are generated by the SAW and would be absent otherwise. Our experimental observations are in good agreement with predictions from micromagnetic simulations that model the ME coupling with an effective time-varying magnetic field which is proportional to the time-varying stress.[15]

## Experimental and Simulation Details

The $LiNbO_3$ substrate on which the magnetostrictive nanomagnets are fabricated is first cleaned in ethanol and the Au electrodes for launching the SAW are delineated using optical lithography. After delineation of the electrodes, the substrate is spin-coated (spinning rate ~2500 rpm) with bilayer polymethyl methacrylate (PMMA) resists of two different molecular weights and subsequently baked at 110 °C for 5 min. Next, electron beam lithography is performed using a Hitachi SU-70 scanning electron

microscope (accelerating voltage of 30 kV, beam current 60 pA) with a Nabity NPGS lithography attachment to open windows for deposition of the nanomagnets. The resists are finally developed in methyl isobutyl ketone and isopropyl alcohol (MIBK-IPA, 1:3) for 270 s, which is followed by a cold IPA rinse. A 5-nm-thick Ti adhesion layer is deposited on the patterned substrate using electron beam evaporation (base pressure ~ $2 \times 10^{-7}$ Torr), followed by the electron beam deposition of 6-nm-thick Co. The lift-off is carried out by remover PG solution.

We have used solid rectangular shaped electrodes to launch SAW in the substrate, instead of the usual inter-digitated transducers (IDT), thereby sacrificing some SAW coupling efficiency, because IDTs are narrow-band filters and our intention was to launch a broad band of SAW frequencies, for which IDTs would not have been functional. A time-varying voltage with frequency in the GHz range is applied between the electrodes which results in a time-varying strain in the region pinched between the electrodes owing to $d_{31}$ and $d_{33}$ coupling. The time varying strain produces an acoustic wave which is very different from the traditional Rayleigh, Sezawa, Lamb or Love modes. We discuss the nature of these waves in Section S-1 of the electronic supplementary material. Figure 1(a) shows the scanning electron microscopy (SEM) image of the nanomagnet array comprising elliptical nanomagnets with major axis dimension ~360 nm, minor axis dimension ~330 nm and thickness ~6 nm. The edge-to-edge separation between the nanomagnets is ~65 nm in the direction of the major axes and ~40 nm in the direction of the minor axes.

The ultrafast magnetization dynamics were measured by a custom-built time-resolved magneto optical Kerr effect (TR-MOKE) microscope[16-18] in a collinear two-color pump-probe setup. The second harmonic (λ = 400 nm, spot size ~1 μm, fluence ~12 mJ cm$^{-2}$) of a Ti-sapphire oscillator was used to excite the dynamics, whereas the time-delayed fundamental laser (λ = 800 nm, spot size ~800 nm, fluence ~1 mJ cm$^{-2}$) was used to probe the dynamics. The probe beam samples approximately four nanomagnets since the lateral dimensions of the nanomagnets is ~350 nm. The polar Kerr rotation was measured by an optical bridge detector as a function of the time delay between the pump and probe beams. A large magnetic field was first applied along the minor axes of the nanomagnets to saturate the magnetization and then removed. The sample was scanned by a piezoelectric x-y-z stage to position the pump and probe beams at the desired location of the sample. RF signal from a signal generator (Rohde & Schwarz SMB100A, frequency range: 100 kHz to 20 GHz) was launched on the sample through high-frequency and low noise coaxial cable (Model No. N1501A-203). The measurement geometry is schematically depicted in Fig. 1(c).

The micromagnetic simulations that were carried out to compare experimental observations with theory were performed using object oriented micromagnetic framework (OOMMF) software[19] on a 7×7 array of nanomagnets, discretizing the samples into rectangular prisms of dimensions 2

× 2 × 6 nm³. First, the static magnetic state was obtained under experimental field configuration. Subsequently, the magnetization dynamics was triggered in the simulation using different excitation fields. The optical excitation was mimicked by a pulsed magnetic field excitation (peak amplitude = 20 Oe and pulse duration = 10 ps) perpendicular to the sample plane, whereas the effect of SAW was mimicked by an additional sinusoidal excitation field (peak amplitude = 5 Oe and frequency corresponding to the SAW frequency) in the direction of the major axis throughout the whole simulation time. This field is related to the generated stress as,

$$H_{stress}(t) = \frac{3\lambda_S \sigma(t)}{2\mu_0 M_S} \qquad (1)$$

where $\mu_0$ is the magnetic permeability of free space, $M_s$ is the saturation magnetization of the nanomagnets (~1 MA m⁻¹), $\lambda_s$ is the saturation magnetostriction and $\sigma(t)$ is the sinusoidal time-varying stress due to the SAW[15].

To calculate the amplitude of the stress $\sigma(t)$, generated by the S AW, we follow the recipe of an earlier work[20] for a plane surface wave:

$$\sigma_{max} = \sqrt{2PZ_0} \; ; Z_0 = \sqrt{c_{11}\rho} \qquad (2)$$

where $P$ is the power in the wave per unit area, $Z_0$ is the characteristic acoustic impedance, $c_{11}$ is the first diagonal element of the elasticity tensor and $\rho$ is the mass density. The cross-sectional area through which the wave passes is the penetration depth times the width of the electrodes. The penetration depth is approximately the wavelength (which varies with the SAW frequency), but we will take its average value to be ~1 μm (which is the wavelength at 6-7 GHz frequency). Therefore, the cross-sectional area of the wave is roughly 1 μm × 2 mm = 2 × 10⁻⁹ m⁻². Since the power coupled into the substrate is 4.5 μW (calculated later), the power per unit cross-sectional area P = 2.25 kW m⁻². For LiNbO₃, $c_{11}$ = 202 GPa and ρ = 4650 Kg m⁻³. This yields $Z_0$ = 9.7 × 10⁸ N.s m⁻³. Therefore, the stress generated is 1.55 MPa. There is a wide spread in the reported values of the saturation magnetostriction of Co, $\lambda_s$ ranging from 30 ppm[21] to 150 ppm[22] Taking the higher value in view of the fact that magnetostriction may increase in nanoparticles[23] and assuming $M_s$ = 1 MA m⁻¹, we obtain from Equation (1) that the amplitude of $H_{stress}$ is 277.5 A m⁻¹ which is about 3.5 Oe. This is of the same order as 5 Oe assumed in the simulation.

Within each nanomagnet, the SAW amplitude is assumed to be spatially invariant and so is the amplitude of the effective magnetic field $H_{stress}$ associated with it. The wavelength of the SAW in the frequency range 1 – 10 GHz is a few hundreds of nm to few micrometers (section S1 of the electronic supplementary material). The major axes of the nanomagnets are ~360 nm while the minor axes are ~330 nm. Hence, at the lower frequencies, the assumption of spatially invariant $H_{stress}$ amplitude is justified since the nanomagnet's lateral dimension is an order of magnitude smaller than the wavelength, but it is definitely questionable at the higher frequencies. Since taking the spatial variation of the amplitude of $H_{stress}(t)$ into account

would have been computationally prohibitive, we ignored this effect, but understand that it could make some difference. Material parameters used in the simulations were gyromagnetic ratio γ = 17.6 MHz Oe⁻¹, anisotropy field $H_k$ = 0 saturation magnetization $M_s$ = 1400 emu cc⁻¹, and exchange stiffness constant $A$ = 3.0 × 10⁶ erg cm⁻¹. The spatial profiles of the SW modes were calculated using an in-house Matlab code named "DOTMAG" [24].

## Results and Discussion

The simulated hysteresis loops of the sample for two mutually perpendicular orientations of the magnetic field are presented in Fig. 1(b). The results are in qualitative agreement with the experimental MOKE loops[25] showing the presence of configurational anisotropy in the sample.

The measured time-resolved reflectivity and Kerr rotation signals in the absence of any bias magnetic field or SAW are shown in Fig. 2(a) and (b), respectively. The fast Fourier transformed (FFT) power spectra of the experimental and simulated time-domain magnetization are shown in Fig. 2(c) and (d), respectively. The FFT power spectrum of the time-resolved reflectivity signal is shown in the inset of Fig. 2(c). The simulated static spin configuration of the nanomagnet array at remanence is shown in the inset of Fig. 2(d). In the absence of any bias magnetic field or SAW, the magnetization of a nanomagnet precesses around an effective magnetic field determined by the strong magnetostatic interaction between nanomagnets in the array, the shape anisotropy, and any stress caused by the differential thermal expansion/contraction of the nanomagnets and the substrate (as a consequence of laser heating). The resulting SW modes are the intrinsic SW modes of the array. The experimental intrinsic SW spectrum (spectrum of Kerr oscillations) reveals four distinct intrinsic SW modes ~3.1 GHz (M1), ~4.2 GHz (M2), ~7.1 GHz (M3) and ~10.2 GHz (M4) with the powers of lower frequency modes M1 and M2 much larger than those of higher frequency modes M3 and M4. Interestingly, the FFT power spectrum of the time-resolved reflectivity signal also shows a dominant peak at around M2 with two weaker peaks at around M1 and M3. However, the time-resolved reflectivity data measured from the bare LiNbO₃ substrate reveals no clear oscillation, exhibiting only a noisy FFT power spectrum as shown in section S2 of the electronic supplementary material. This is probably due to the fact that the laser heating and cooling effect sets up noisy strain-field oscillations in the bare substrate, which are captured in the reflectivity data. If there is any signal submerged in the measured data, we do not have sufficient sensitivity to capture it.

Before simulating the intrinsic SW dynamics of the nanomagnet array to compare with experiments, we have simulated the intrinsic SW dynamics of a single isolated Co nanomagnet as shown in section S3 of the electronic supplementary material. The static spin configuration of a single

nanomagnet forms an 'S' state and its simulated SW spectrum reveals four clear modes whose spatial profiles show standing wave patterns along the major axis. The axes of quantization of the modes are rotated owing to the asymmetric 'S' state spin configuration. However, the static spin configuration is significantly modified in the multi-nanomagnet array with the spins inside the nanomagnets getting aligned primarily along the major (easy) axes of the nanomagnets (inset of Fig. 2(d)). The simulated SW spectrum of the array again shows four clear peaks in qualitative agreement with the experimental spectrum (Fig. 2(c) and (d)). The slight discrepancies between the theoretical and experimental peak frequencies can be attributed to the difficulty of precisely accounting for the roughness and edge deformations of the real sample in the micromagnetic simulation. The spatial profiles of the simulated intrinsic SW modes of the array are shown in Fig. 2(e). The modes M1, M2 and M3 form standing wave patterns along the major axis with quantization numbers n = 3, 4 and 6, respectively. The highest frequency intrinsic mode M4 has a complex character with mixed quantization along both major (mode quantization number $n = 6$) and minor (mode quantization number $m = 2$) axes of the nanomagnet. We notice that the deformed SW patterns in the single nanomagnet become more symmetric in the array due to the strong interelement magnetostatic coupling.

**SAW driven dynamics:** Finally, we apply SAW to the sample in the geometry shown in Fig. 1(c) with varying frequencies ($f_{SAW}$) in the range, 1 GHz ≤ $f_{SAW}$ ≤ 10 GHz at a fixed input power $P_{SAW}$ = -10 dBm (0.1 mW). Because of impedance mismatch between the source and the sample, most of the input power is reflected back into the source and a small fraction is coupled into the piezoelectric substrate to launch the SAW. Earlier we had measured the $S_{11}$ scattering parameter up to 2.5 GHz.[25] Since we had not measured it across the entire frequency range of interest, we will assume (for the sake of qualitative comparison with experimental data) that the average $S_{11}$ parameter in the frequency range of interest is -0.2 dB (based on the data in ref. 25), which means that only about 4.5% of the incident power is being coupled into the sample. In other words, the power coupled into the SAW is about 4.5 µW.

The SAW propagates along the major axes of the nanomagnets. Figure 3(a) shows the experimental SW spectra after the application of SAW. The simulated SW spectra corresponding to this case was obtained with a sinusoidal time-varying magnetic field $H_{stress}$, as described earlier, applied along the major axis of the nanomagnets to replicate the time-varying stress field caused by the SAW. The simulation results (Fig. 3(b)) are in good qualitative agreement with the experimental SW spectra. The launched SAW periodically expands and contracts the Co nanomagnets and modifies their magnetization precession owing to the inverse magnetostrictive (Villari) effect.

**Non-resonant excitation:** When the SAW frequency is not resonant with any intrinsic mode frequency, the SAW would generate a new ME mode at its own frequency. These are the extrinsic modes which are synchronous with the SAW. For

example, at $f_{SAW}$ = 1 GHz, a new (extrinsic) mode appears at ~1 GHz in addition to the existing intrinsic SW modes. This new mode was not present in the absence of the SAW and is therefore generated exclusively by the SAW. However, characterization of precise elastic and magnetic components present in this mode is beyond the scope of this article.[26] Nevertheless, this is an exciting observation since the new SW mode would couple to a radiating electromagnetic wave and therefore radiate an electromagnetic wave of the same frequency as the driving SAW. This is the basis of a microwave frequency (1 GHz) magnetoelastic antenna.[25]

**Resonant Excitation:** When the SAW frequency is resonant with one of the intrinsic SW mode frequencies, the SAW drives the nanomagnets into ME resonance, amplifying the power of that intrinsic mode significantly. This type of resonance phenomenon has been predicted theoretically from micromagnetic simulations.[27] At $f_{SAW}$ = 3 GHz (4 GHz), the power of M1 (M2), which is resonant with the SAW, is amplified while other modes are suppressed. Consequently, we observe a SW spectrum having one dominant resonantly amplified mode with a low power shoulder on the left or the right side. The frequencies of the suppressed modes M3 and M4 are actually resonant with $f_{SAW}$ = 7 GHz, and 10 GHz respectively, and hence, their powers are significantly amplified at those SAW frequencies. On the other hand, when $f_{SAW}$ is adjacent to M3 (6 GHz or 8 GHz), it excites an extrinsic mode at the SAW frequency by nearly annihilating M3, as shown by the red dotted box in Fig. 3(a) and b. These observations show that we can always generate SW modes at the frequency of the SAW and if the latter happens to be resonant with an intrinsic SW mode (i.e. a mode which is present in the absence of SAW), then that mode is amplified by the SAW.

Fig. 3(c) shows the calculated power and phase profiles of selected modes after the application of SAW (calculated with DOTMAG [24]). The power and phase profiles of the SW modes whose frequencies are resonant with the SAW frequencies become more uniform upon application of SAW (as shown in Fig. 3(c) for M* and M3 and Fig. S4 of the supplemental materials for M1, M2 and M4). Therefore, the SAW has a smoothing effect on the profiles of those modes that it drives resonantly. However, the nature of those modes, including mode quantization number, remains unaffected. The SAW-generated new extrinsic modes at 6 and 8 GHz also exhibit standing wave pattern along the major axis of the ellipse with mode quantization number $n = 5$ and 7, respectively, as shown in Fig. 3(c).

In order to check (theoretically) for possible anisotropic nature of the SAW coupling with SW (magnon-phonon coupling), we have further simulated the SW dynamics of the array at remanence with the sinusoidal field $H_{stress}(t)$ applied along the minor axis of the elliptical nanomagnets. Fig. 4(a) shows the simulated time-domain magnetization ($M_z(t)$) at three different frequencies of $H_{stress}(t)$ and Fig. 4b shows the corresponding FFT power spectra. A drastic change in the SW spectra is observed with a single dominant extrinsic SW mode appearing at the

frequency of the SAW in all three cases. The intrinsic SW modes of the array at remanence are completely annihilated when excited by SAW in this geometry and replaced by the extrinsic mode. This shows the strongly anisotropic nature of the SAW coupling. This is also a very exciting result since it shows that in this configuration, it may be possible to implement a nearly 'monochromatic' magnetoelastic antenna which would be radiating almost exclusively at the SAW excitation frequency without any sideband. In future, we will verify this result experimentally.

The magnon-phonon coupling (between SW and SAW) studied here is not necessarily optimal. Optimal coupling requires phase matching between the two waves where the wavevectors of the two waves will be equal. We do not currently know the wavevectors of the SW at the SAW frequencies since we do not know their dispersion relations. We are obtaining these dispersion relations using Brillouin light scattering (BLS) and would attempt to study phase matching scenarios in the future.

In order to gain more insight into the observed dynamics, we have further simulated the magnetostatic field distribution of the array by using LLG micromagnetic simulator[28]. Fig. 4(c) shows the contour plots of the magnetostatic fields of the nanomagnet array at remanence. The arrows represent the magnetization inside the dots. Strong inter-element interacting field lines are observed along the major axes of the nanomagnets, indicating dominant dipolar contribution from the magnetostatic stray field along this direction. To quantify the inter-element interaction, we have taken line scans of the magnetostatic fields along both major and minor axes of the nanomagnets as shown by the black dotted lines in Fig. 4(c). From Fig. 4(d), it is evident that the magnitude of the inter-element stray field along the major axes is ~2.2 kOe, whereas, along the minor axes it is negligibly small. This indicates stronger inter-element interaction along the major axes than along the minor axes of the nanomagnets, despite the fact that the center-to-center separation between nearest neighbor nanomagnets in the array is 425 nm along the major axis and smaller (370 nm) along the minor axis. This is due to the abundance of free magnetic poles at the edges of the nanomagnets along the major axis, which causes a significantly large stray magnetic field along that direction. Along the minor axis, the free magnetic poles are negligible causing negligibly small stray magnetic field. This property (anisotropic dipole interaction in a 2D array) has been exploited in devising nanomagnet-based computing platforms, such as image processors[29] and anti-correlators/correlators for Bayesian networks[30]. Here, the anisotropy makes the extrinsic (SAW-driven) SW dynamics very different along the two directions.

## Conclusions

In conclusion, the magnetodynamics in a densely packed 2D array of elliptical Co magnetostrictive nanomagnets fabricated on a piezoelectric LiNbO$_3$ substrate has been probed in the absence of any bias magnetic field and without/with SAW excitation. A SAW launched into the array amplifies the intrinsic SW modes if their frequencies are resonant with the applied SAW frequencies. New SW (extrinsic) modes are spawned by the SAW at the SAW frequencies when they are not resonant with the intrinsic modes. The coupling between SW and SAW is highly anisotropic in nature. All observed features are qualitatively reproduced by micromagnetic simulations. Our findings provide fundamental insight into bias-field free magnonics[31], which offer exciting potentials for the design of energy efficient spin-wave filters and strain-controlled magnonic nano-devices.

## Author Contributions

A.B. and Su.B. planned and supervised the project. J.L.D. fabricated the samples. A.D. performed the time-resolved magneto-optical measurements, micromagnetic simulations and analyzed the data. Sa.B. helped in performing the LLG micromagnetic simulation. A.B. and Su.B. wrote the manuscript in consultation with other co-authors.

## Conflicts of interest

The authors state no potential conflict of interest.

## Acknowledgements

## References

1 W. Rushforth, E. De Ranieri, J. Zemen, J. Wunderlich, K.W. Edmonds, C.S. King, E. Ahmad, R. P. Campion, C. T. Foxon, B. L. Gallagher, K. Výborný, J. Kučera, T. Jungwirth, *Phys. Rev. B* 2008, **78**, 085314.

2 M. Weiler, L. Dreher, C. Heeg, H. Huebl, R.Gross, M. S. Brandt, S. T. B. Goennenwein, *Phys. Rev. Lett.,* 2011, **106**, 117601.

3 A. V. Scherbakov, A. S. Salasyuk, A. V. Akimov, X. Liu, M. Bombeck, C. Bruggemann, D. R. Yakovlev, V. F. Sapega, J. K. Furdyna, M. Bayer, *Phys. Rev. Lett.*, 2010, **105**, 117204.

4 M. Bombeck, A. S. Salasyuk, B. A. Glavin, A. V. Scherbakov, C. Bruggemann, D. R.Yakovlev, V. F. Sapega, X. Liu, J. K. Furdyna, A. V. Akimov, M. Bayer, *Phys. Rev. B,* 2012, **85**, 195324.

5 A. Barman, S. Mondal, S. Sahoo, A. De, *J. Appl. Phys.,* 2020, **128**, 170901.

6 A. Biswas, S. Bandyopadhyay, J. Atulasimha, *Appl. Phys. Lett.,* 2013, **103**, 232401.

7 V. Sampath, N. D'Souza, D.  Bhattacharya, G. M.  Atkinson, S. Bandyopadhyay, J. Atulasimha, *Nano Lett.,* 2016, **16**, 5681–5687.

8 C. Berk, M. Jaris, W. Yang, S. Dhuey, S. Cabrini, H. Schmidt, *Nat. Commun.,* 2019, **10**, 2652.

9 Z. Xiao, R. Lo Conte, M. Goiriena-Goikoetxea, R. V. Chopdekar, C.-H. A. Lambert, X. Li, A. T. N'Diaye, P. Shafer, S. Tiwari, A. Barra, A. Chavez, K. P. Mohanchandra, G. P. Carman, K. L. Wang, S. Salahuddin, E. Arenholz, J. Bokor, R. N. Candler, *ACS Appl. Mater. Interfaces,* 2020, 12, 6752–6760.

10 W. Edrington, U. Singh, M. A.  Dominguez, J. R. Alexander, R. Nepal, S. Adenwalla, *Appl. Phys. Lett.,* 2018, 112, No. 052402.

11 S. Davis, A. Baruth, S. Adenwalla, *Appl. Phys. Lett.,* 2010, 97, No. 232507.

12 M. Foerster, F. Macia, N. Statuto, S. Finizio, A. S. Hernandez-Mínguez, S. Lendínez, P. V. Santos, J. Fontcuberta, J. M. Hernàndez, M. Klaui, L. Aballe, *Nat. Commun.,* 2017, 8, 407.

13 Y. Yahagi, B. Harteneck, S. Cabrini, H. Schmidt, *Phys. Rev. B,* 2014, 90, 140405 (R).

14 S. Mondal, M. A. Abeed, K. Dutta, A. De, S. Sahoo, A. Barman, S. Bandyopadhyay, *ACS Appl. Mater. Interfaces,* 2018, 10, 43970-43977.

15 M. S. Fashami, J. Atulasimha, S. Bandyopadhyay, *Nanotechnology,* 2012, 23, 105201.

16 A. Barman, A. Haldar, *Solid State Phys*, 2014, 65, 1–108.

17 A. Barman, J. Sinha, *Springer International Publishing AG*, 2018.

18 S. Pal, S. Saha, M. V. Kamalakar, A. Barman, *Nano Research,* 2016, 9(5), 1426–1433.

19 M. Donahue, D. G. Porter, OOMMF User's guide, Version 1.0, Interagency Report NISTIR 6376, National Institute Standard and Technology, Gaithersburg, MD (1999); http://math.nist.gov/oommf.

20 S. Datta, Prentice Hall, Englewood Cliffs, New Jersey, 1986.

21 Z. Nishiyama, *Sci. Rep. Tohoku Imp. Univ. Ser.* 1 1929, 18, 341.

22 R. M. Bozorth, *Phys. Rev.,* 1954, 96, 311-316.

23 S. J. Zhao, *Nanomaterials,* 2015, 1-12.

24 D. Kumar, O. Dmytriiev, S. Ponraj, A. Barman, *J. Phys. D: Appl. Phys.,* 2012, 45, No. 015001.

25 J. L. Drobitch, A. De, K. Dutta, P. K. Pal, A. Adhikari, A. Barman, S. Bandyopadhyay, *Adv. Mater. Tech.,* 2020, 5, No. 2000316.

26 F. Vanderveken, J. Mulkers, J. Leliaert, B. Van Waeyenberge, B. Sor´ee, O. Zografos, F. Ciubotaru, C. Adelmann, arXiv:2011.10326 [cond-mat.mes-hall].

27 W. A. Misba, M. M. Rajib, D.  Bhattacharya, J. Atulasimha, *Phys. Rev. Appl.,* 2020, 14, 014088.

28 LLG Micromagnetics Simulator, developed by M. R. Scheinfein http://llgmicro.home.mindspring.com (accessed March 8, 2018).

29 M. A. Abeed, A. K. Biswas, M. M. Al-Rashid, J. Atulasimha, S. Bandyopadhyay, *IEEE Trans. Elec. Dev.,* 2017, 64, 2417-2424.

30 M. T. McCray, M. A. Abeed, S. Bandyopadhyay, *Sci. Rep.,* 2020, 10, No. 12361.

31 A. Haldar, D. Kumar, A. O. Adeyeye, *Nature Nanotechnol.,* 2016, 11, 437–443.
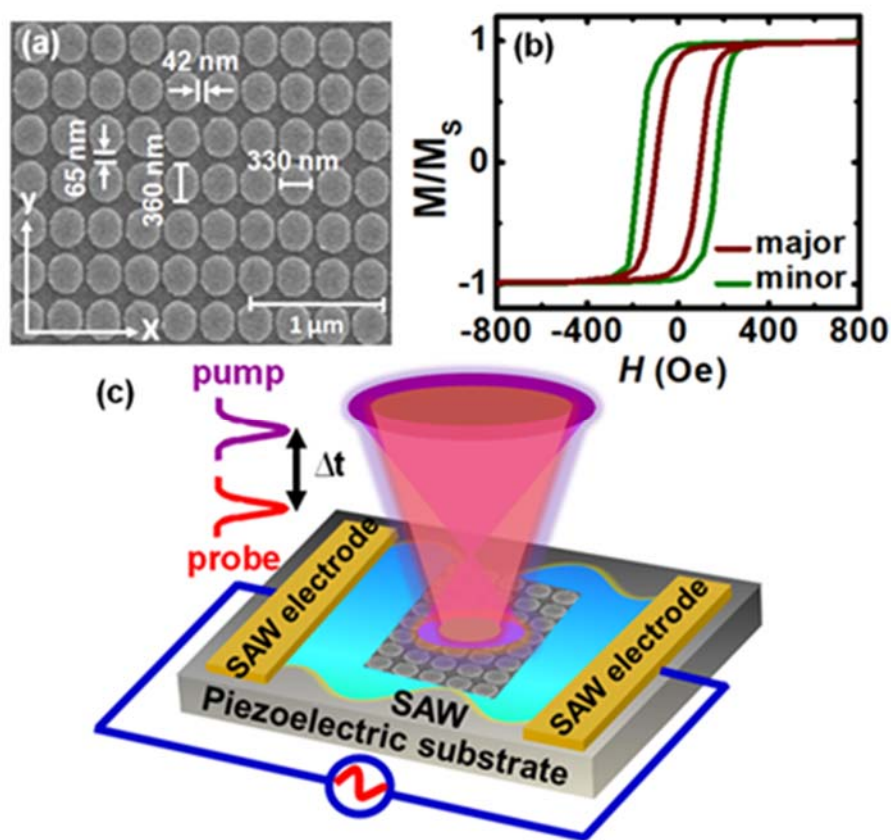
**Figure 1:** (a) Scanning electron microscopy (SEM) image of the nanomagnet array. (b) Simulated magnetic hysteresis loop of the sample which are in qualitative agreement with the measured loops in ref. [25] (c) Schematic of the measurement geometry showing the launched SAW along with the pump and probe beams of the TR-MOKE measurement.
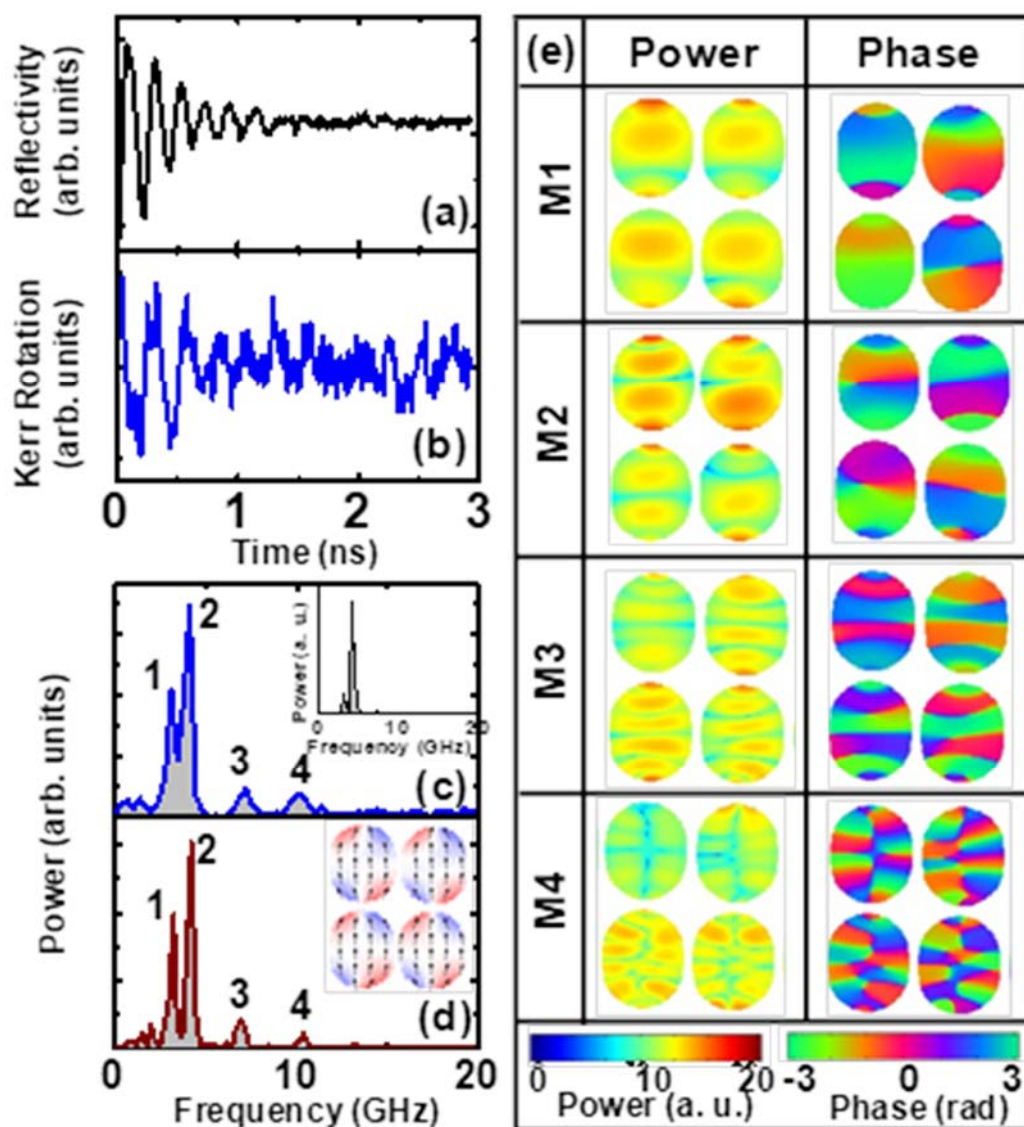
**Figure 2:** Background subtracted experimental time-resolved (a) reflectivity and (b) Kerr rotation data in the absence of SAW and any bias magnetic field. (c) FFT power spectrum of the experimental time-resolved Kerr rotation (FFT of time-resolved reflectivity in the inset). (d) FFT power spectrum of simulated time-resolved magnetization showing excellent agreement with the experimental data in 2(c). The simulated static magnetic configuration of a part of the nanomagnet array at remanence is shown in the inset. (e) Power and phase profiles of the SW modes of the nanomagnet array. The corresponding color bars are shown in the figure.
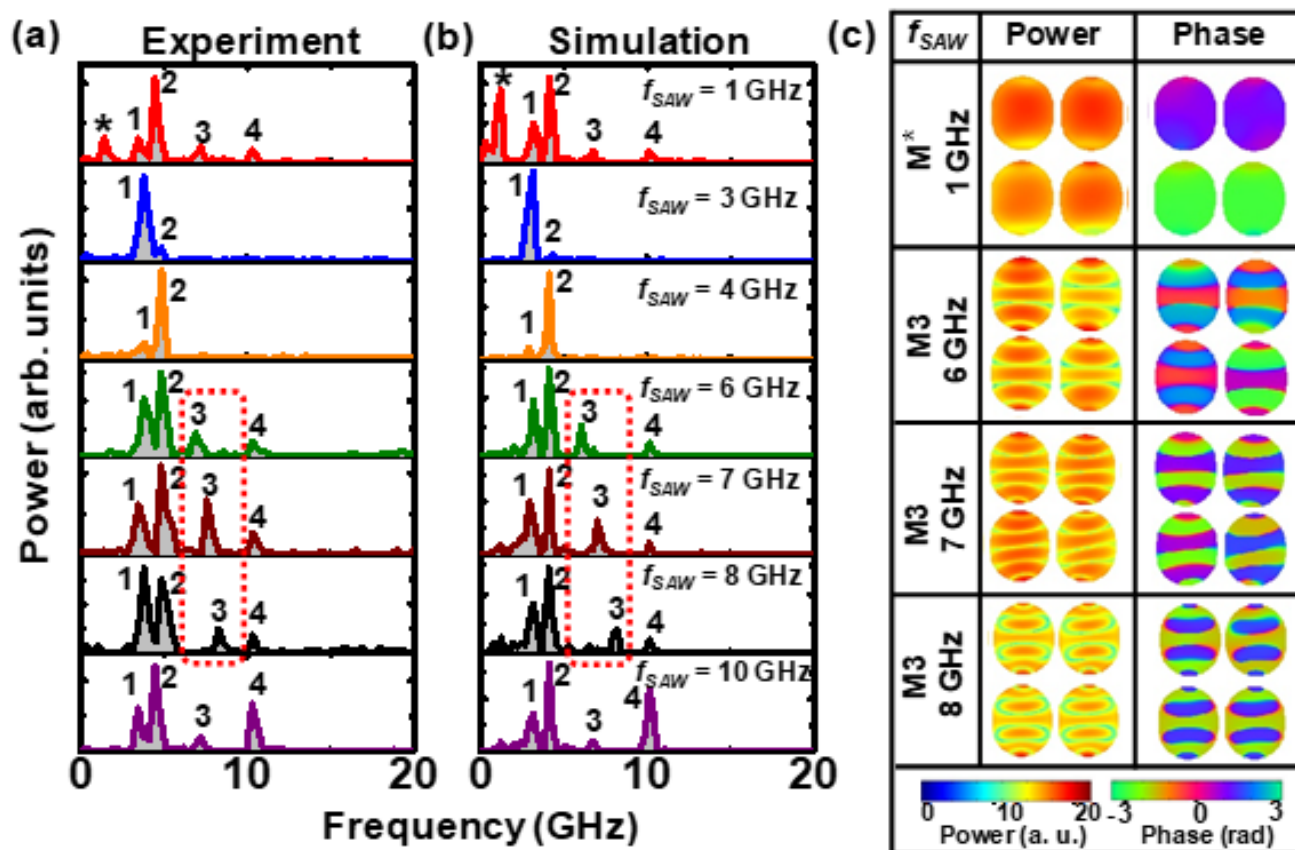
**Figure 3:** (a) The experimental and (b) simulated SW spectra of the nanomagnet array at different values of SAW frequency $f_{SAW}$, with SAW propagation along the major axis of the nanomagnets (c) The power and phase profiles of selected SW modes at different values of $f_{SAW}$. The color bars are shown at the bottom.
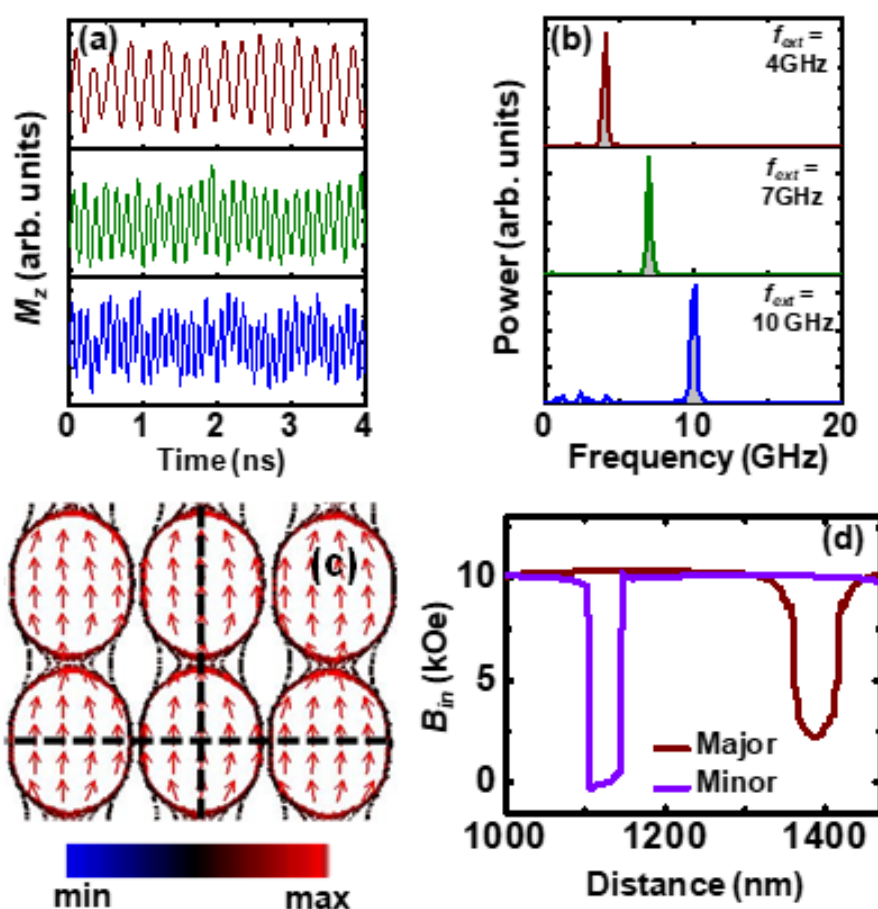
**Figure 4:** (a) Simulated time-domain magnetization ($M_z$) when the sinusoidal field mimicking the SAW is applied along the minor axes of the nanomagnets (corresponding to SAW propagation along the minor axis) and (b) the corresponding FFT power spectra. (c) Contour plot of the simulated magnetostatic field distribution of the nanomagnet array at remanence and (d) line scans of the magnetostatic field taken along the black dotted lines as shown in (c). The color bar is shown below the plot in (c).